

Computational Microscopy beyond Perfect Lenses

Xingyuan Lu^{1,2}, Minh Pham^{1,3}, Elisa Negrini³, Damek Davis⁴, Stanley J. Osher³, and Jianwei

Miao^{1*}

¹Department of Physics & Astronomy and California NanoSystems Institute, University of California, Los Angeles, CA 90095, USA.

²School of Physical Science and Technology, Soochow University, Suzhou 215006, China.

³Department of Mathematics, University of California, Los Angeles, CA 90095, USA.

⁴School of Operations Research and Information Engineering, Cornell University, Ithaca, NY 14850, USA.

Lens-based microscopy has played an important role in the evolution of modern science and technology. The development of coherent diffractive imaging (CDI) in 1999 that replaces the lens with coherent illumination and computational algorithms has transformed our conventional view of microscopy. Here we demonstrate through mathematical analysis and numerical experiments that in situ CDI, which harnesses the coherent interference between a strong beam illuminating a static structure and a weak beam illuminating a dynamic structure, could be the most dose-efficient imaging method. At low doses, in situ CDI can achieve higher resolution than perfect lenses with the point spread function as a delta function. We expect that computational microscopy based on in situ CDI can be implemented in different imaging modalities with photons and electrons for low-dose imaging of radiation-sensitive materials and biological samples.

The resolution of microscopy is set by the point spread function (PSF) [1]. A microscope with the PSF assumed to be a delta function would represent a perfect imaging system. The other

factor affecting the resolution of microscopy is the illumination, that is, the number of photons or electrons used to form an image. Without illumination, no image can be produced by any microscope. When there is unlimited illumination, a perfect microscope would be an ultimate imaging system. However, many important systems such as energy materials, catalysts, polymers, and biological samples are very sensitive to x-rays or electrons, which is known as radiation damage effects [2-5]. In this Letter, we use mathematical analysis and numerical experiments to show that at low doses, computational microscopy based on in situ CDI can outperform microscopy with perfect lenses. CDI is a lensless imaging technique with the resolution only limited by the diffraction signal [6]. Over the years, CDI methods, such as plane-wave CDI, Bragg CDI and ptychography (i.e., scanning CDI), have been broadly implemented using synchrotron radiation, x-ray free electron lasers, high harmonic generation, electron and optical microscopy [7-28]. However, although CDI methods have overcome the resolution limit set by the lens, their application to radiation-sensitive samples remains challenging. An approach to improve CDI's dose- efficiency is to incorporate strong scatterers in the vicinity of weakly scattering or biological samples [29-34]. More recently, numerical experiments have indicated that in situ CDI can significantly reduce the radiation dose by 1-2 orders of magnitude over conventional CDI [35]. However, the mathematical foundation on the radiation dose reduction of in situ CDI is unknown. Here we use mathematical analysis and numerical experiments to demonstrate that in situ CDI could be the most dose-efficient imaging method and at low doses, can achieve higher resolution than microscopy with perfect lenses.

In situ CDI takes advantage of the coherent interference from a static and a dynamic structure [Fig. 1(a)]. Let's define Ψ_S and Ψ_D as the Fourier transform of the static and the dynamic

structure, respectively, where for simplicity we omit the reciprocal space coordinates and the time variable in the dynamic structure. We first consider conventional CDI without the static structure. The diffraction intensity of the dynamic structure is,

$$I_0 \left(\frac{r_e \lambda}{l_D \sigma_D} \right)^2 |\Psi_D|^2 = I_D \quad (1)$$

where I_0 is the fluence (photons per unit area) of the incident wave on the dynamic structure, r_e is the classical electron radius, λ is the wavelength, I_D is the diffraction intensity (photons per pixel), l_D and σ_D are the size and the linear oversampling ratio of the dynamic structure [36], respectively. We rewrite Eq. (1) as,

$$\tilde{D} \equiv \frac{r_e \lambda \sqrt{I_0}}{l_D \sigma_D} \Psi_D, \quad |\tilde{D}|^2 = I_D \quad (2)$$

Eq. (2) can be represented as a circle in the complex plane [Fig. 2(a)]. Although Eq. (2) is a non-convex problem, a unique solution [the red dot in Fig. 2(a)] can be solved by iterative phase retrieval algorithms [37], provided that the fluence is sufficiently high and the oversampling condition is satisfied [36]. However, when the fluence is very low, the circle becomes an annulus with the width of the ring set by the Poisson noise in the diffraction intensity [Fig. 2(b)]. The presence of very high Poisson noise will make iterative algorithms trapped in local minima instead of converging to the global minimum [37].

An approach to overcome this major limitation is in situ CDI [Fig. 1(a)], which is mathematically represented by,

$$\left| \frac{r_e \lambda \sqrt{I_1}}{l_S \sigma_S} \Psi_S + \frac{r_e \lambda \sqrt{I_0}}{l_D \sigma_D} \Psi_D \right|^2 = I \quad (3)$$

where I_1 is the fluence of the incident wave on the static structure with $I_1 \gg I_0$, I is the diffraction intensity, l_s and σ_s are the size and the linear oversampling ratio of the static structure [36], respectively. We rewrite Eq. (3) as,

$$\tilde{S} \equiv \frac{r_e \lambda \sqrt{I_1}}{l_s \sigma_s} \psi_s, \quad |\tilde{S} + \tilde{D}|^2 = I \quad (4)$$

As $|\tilde{S}| \gg |\tilde{D}|$, Eq. (4) can be represented by the intersection of a large circle and a small annulus in the complex plane [Fig. 2(c)]. Due to the very low Poisson noise in I , iterative phase retrieval algorithms can be used to find the global solution of $\tilde{S} + \tilde{D}$ [i.e. the red dot in Fig. 2(c)] instead of trapping in local minima. To mathematically solve Eq. (4), we define,

$$\tilde{S} = \mathcal{F}S = \mathcal{F}_r S + i\mathcal{F}_i S, \quad \tilde{D} = \mathcal{F}D = \mathcal{F}_r D + i\mathcal{F}_i D \quad (5)$$

where \mathcal{F} is the Fourier transform, S and D are the static and dynamic structure, $\mathcal{F}_r S$ and $\mathcal{F}_i S$ are the real and imaginary part of $\mathcal{F}S$, respectively. Substituting Eq. (5) into Eq. (4) and ignoring the very small $|\tilde{D}|^2$ term, we have

$$\mathcal{F}_r S \mathcal{F}_r D + \mathcal{F}_i S \mathcal{F}_i D \approx \frac{1}{2} (I - |\tilde{S}|^2) \quad (6)$$

where S can be accurately retrieved from the diffraction pattern due to the illumination of a high fluence on the static structure. Let's assume the array size of D and I to be $n \times n$ and $N \times N$, respectively. Since D is complex and I is real, with $N^2 > 2n^2$, there are more independent equations than the unknown variables [36]. To solve Eq. (6), we convert it to the matrix form,

$$AD = b \quad (7)$$

$$A = \text{diag}(\mathcal{F}_r S) \mathcal{F}_r + \text{diag}(\mathcal{F}_i S) \mathcal{F}_i \quad b = \frac{1}{2} (I - |\tilde{S}|^2)$$

where A is a diagonal matrix with dimension $N^2 \times N^2$, D has dimension $N^2 \times 1$ after padding with zeros, and b has dimension $N^2 \times 1$. Eq. (7) can be solved by the least square method, $\min_D \frac{1}{2} \|AD - b\|^2$,

$$D = (A^T A)^{-1} A^T b \quad (8)$$

where A is assumed to have independent columns, superscripts T and -1 represent the transpose and inverse of a matrix.

To compare in situ CDI with a perfect imaging system, we simulate Zernike phase-contrast microscopy with perfect lenses [38], which assumes the PSF to be a delta function [Fig. 1(b)]. For a weak phase object in Zernike phase-contrast microscopy, the intensity (I_z) of the complex exit wave can be approximated as

$$I_z = a^2 \pm 2a\varphi \quad (9)$$

where the amplitude of the unscattered wave is reduced by a factor of a , φ is the phase shift of the sample, and the \pm sign indicates a positive ($\frac{\pi}{2}$) and a negative ($-\frac{\pi}{2}$) phase shift [39]. In our numerical experiment, we first simulate a dynamic biological vesicle of protein complexes and water, consisting of 20 frames with a thickness of 100 nm and a pixel size of 11.4 nm (Supplemental Material [40], Video S1 and Table S1). Using Eq. (9), we calculate the intensity of the phase-contrast images of the vesicle with varying x-ray fluences, where the PSF is assumed to be a delta function. Figure 3(a)-(d) and Video S2(a) show the representative phase-contrast images with a fluence of $3.5e5$, $3.5e6$, $3.5e7$, and $3.5e8$ photons/ μm^2 and Poisson noise, respectively, produced by Zernike phase-contrast microscopy with perfect lenses. To examine the effect of the pixel size on the resolution, we create biological vesicles with a pixel size of 1, 5 and 10 nm and

calculate their phase-contrast images with perfect lenses (Fig. S1 in Supplemental Material [40]), indicating that at these low doses, the resolution is not limited by the pixel size, but the dose.

We then use the time-varying biological vesicle as the dynamic structure and a 20-nm-thick Au pattern as the static structure (Fig. S2 in Supplemental Material [40]). With an x-ray energy of 530 eV, we calculate a time-sequence diffraction patterns from the complex exit waves of both the dynamic and static structures using Eq. (4), whereas the fluence on the static structure is 1.4×10^{11} photons/ μm^2 and the fluence on the dynamic structure varies from 3.5×10^5 , 3.5×10^6 , 3.5×10^7 to 3.5×10^8 photons/ μm^2 . Poisson noise is added to the diffraction patterns and the oversampling ratio of the static and dynamic structure is 8 [36]. To reconstruct both the static and dynamic structure, we apply iterative phase retrieval algorithms to Eq. (4), which is more accurate than Eq. (8). We first reconstruct the static structure of the 20-nm-thick Au pattern from the diffraction patterns by combining the hybrid input-output algorithm [41] with shrinkwrap [42]. We then apply the static structure as a time-invariant constraint to retrieve the amplitudes and phases of the dynamic biological vesicle at different fluences using the generalized proximal smoothing algorithm [43]. We further improve the static structure during the phase retrieval of the time-sequence diffraction patterns [35], in which the illumination function of the incident wave can also be incorporated if desired. Figure 3(e)-(h) and Video S2(b) show the representative phase images of in situ CDI with a fluence of 3.5×10^5 , 3.5×10^6 , 3.5×10^7 , and 3.5×10^8 photons/ μm^2 , respectively. Using the Fourier shell correlation (FSC), we quantitatively compare the phase images between in situ CDI and perfect lenses [Fig. 3(i)], showing that in situ CDI produces slightly higher-resolution phase images than the perfect lenses.

Next, we increase the thickness of the dynamic biological vesicle to 300 nm (Table S1 in Supplemental Material [40]). Using Eq. (9), we calculate the phase-contrast images with a fluence of $3.5e5$, $3.5e6$, $3.5e7$, $3.5e8$ photons/ μm^2 and Poisson noise [Fig. S3(a)-(d) in Supplemental Material [40], Video S2(c)]. For comparison, we use the same phase-retrieval procedure of in situ CDI to reconstruct the amplitudes and phases of the dynamic biological vesicle using Eq. (4), whereas the fluence on the dynamic structure varies from $3.5e5$, $3.5e6$, $3.5e7$ to $3.5e8$ photons/ μm^2 and the fluence on the static structure is fixed at $1.4e11$ photons/ μm^2 . Figure S3(e)-(h) in Supplemental Material [40] and Video S2(d) show the representative phase images of the biological vesicle. FSC comparisons indicate that in situ CDI produces slightly higher-resolution phase images than the perfect lenses [Fig. S3(i) in Supplemental Material [40]], which is due to the fundamental difference of the imaging mechanism between the two methods. In situ CDI takes advantage of the coherent interference from all the pixels in the static and dynamic structure, from which a global solution of the complex wave (i.e., both the amplitude and phase of the sample) is reconstructed [Fig. 2(c)]. For a given fluence, the increase of the sample thickness improves the signal to noise ratio of the reconstructed images. On the other hand, Zernike phase-contrast microscopy with perfect lenses forms images locally, that is, every pixel is independent of other pixels. Additionally, Eq. (9) assumes a weak phase approximation (i.e., $\varphi \ll 1$). With the increase of the sample thickness, the weak phase approximation becomes inaccurate.

To further illustrate this point, we increase the thickness of the dynamic biological vesicle to 1 μm (Supplemental Material [40], Table S1). Under such a condition, Zernike phase-contrast microscopy cannot produce phase images as Eq. (9) does not hold any more. To acquire images from thick biological samples, we employ absorption-contrast microscopy with perfect

lenses with the PSF as a delta function. Figure 4(a)-(d) shows four representative images with a fluence of $3.5e4$, $3.5e5$, $3.5e6$, $3.5e7$ photons/ μm^2 and Poisson noise, respectively. In contrast, in situ CDI can simultaneously reconstruct the amplitude and phase of the complex wave without the thickness limitation. Using the same phase retrieval procedure, we obtain the phase images for the 1- μm -thick biological vesicle with a fluence of $3.5e4$, $3.5e5$, $3.5e6$, and $3.5e7$ photons/ μm^2 [Fig. 4(e)-(h)]. Quantitative FSC comparisons indicate that for thick biological samples, the phase images of in situ CDI requires an order of magnitude lower dose than the absorption-contrast images with perfect lenses [Fig. 4(i)]. To test the convergence of in situ CDI with the lowest possible dose, we reduce the fluence to $1.75e3$, $3.5e3$, $6.2e3$ and $7.7e3$ photons/ μm^2 . Figure S4 in Supplemental Material [40] shows that even with a fluence of $1.75e3$ photons/ μm^2 (i.e., 0.23 photon/pixel and a dose of 137.5 Gy), the biological vesicle is still faintly visible in the phase image of in situ CDI.

Phase retrieval from the diffraction intensity in CDI is intrinsically a non-convex problem. Over the years, a number of phase retrieval algorithms have been developed to solve this non-convex problem [37], provided there are sufficient signal to noise ratios in the diffraction intensity and the number of independent measurement points are larger than that of unknown variables [36]. However, when the signal to noise ratio is very low, phase retrieval algorithms are usually trapped in local minima, instead of converging to the global minimum [37]. Here, we demonstrate through mathematical analysis that in situ CDI can overcome this local minima problem by taking advantage of the coherent interference between a strong and a weak beam illuminating a static and a dynamic structure, respectively. Our numerical experiments show that in situ CDI can not only achieve higher resolution than perfect lenses at low doses, but also perform

successful phase retrieval with an average fluence on the sample as low as 0.23 photon/pixel. Compared with ptychography that uses spatial overlap structures as a constraint [11,12], in situ CDI employs temporal overlap structures as a constraint [35], enabling us to capture dynamic phenomena at higher temporal resolution. In situ CDI can also be combined with ptychography to increase the field of view. Compared with Fourier holography that requires the exact knowledge of the reference wave with the resolution set by the reference source size [44,45], in situ CDI is fundamentally different and more efficient as it reconstructs both the static and dynamic structures from a time-sequence diffraction patterns with the resolution only limited by the diffraction signal. In combination with coherent x-ray sources such as diffraction-limited storage ring, x-ray free electron lasers and high harmonic generation [21,46] as well as bright electron sources [47], in situ CDI could become a powerful dose-efficient imaging method to probe the structure and dynamics of a wide range of radiation-sensitive materials and biological samples.

This work was supported by STROBE: a National Science Foundation Science and Technology Center under award no. DMR-1548924 and the U.S. Air Force Office Multidisciplinary University Research Initiative (MURI) program under award no. FA9550-23-1-0281. M.P. and E.N. acknowledge the support by Simons Postdoctoral program at IPAM and DMS1925919. D.D. acknowledges the support by an Alfred P. Sloan research fellowship and NSF DMS award 2047637.

X.L. and M.P. contributed equally to this work. J.M. conceived the idea and directed the project; M.P., J.M., E.N., D.D., S.J.O. discussed and/or carried out the mathematical analysis; X.L., M.P., E.N. and J.M. discussed and/or performed the numerical experiments; J.M. wrote the manuscript with input from X.L., M.P. and E.N. All authors commented on the manuscript.

*Email: miao@physics.ucla.edu

Reference:

1. E. Wolf (ed.), *Progress in Optics*, vol. 51, pp. 355, Elsevier (2008).
2. R. Henderson, *Q. Rev. Biophys.* **28**, 171 (1995).
3. R. F. Egerton, P. Li, and M. Malac, *Micron* **35**, 399 (2004).
4. Howells et al., *J. Electron Spectros. Relat. Phenomena* **170**, 4 (2009).
5. M. Du, and C. Jacobsen, *Ultramicroscopy* **184**, 293 (2018).
6. J. Miao, P. Charalambous, J. Kirz, and D. Sayre, *Nature* **400**, 342 (1999).
7. J. Miao et al., *Phys. Rev. Lett.* **89**, 088303 (2002).
8. D. Shapiro et al., *Proc. Natl. Acad. Sci. U.S.A.* **102**, 15343 (2005).
9. M. A. Pfeifer et al., *Nature* **442**, 63 (2006).
10. H. N. Chapman *et al.*, *Nat. Phys.* **2**, 839 (2006).
11. J. M. Rodenburg et al., *Phys. Rev. Lett.* **98**, 034801 (2007).
12. P. Thibault et al., *Science* **321**, 379 (2008).
13. C. Song et al., *Phys. Rev. Lett.* **101**, 158101 (2008).
14. I. Robinson and R. Harder, *Nat. Mater.* **8**, 291 (2009).
15. K. Giewekemeyer et al. *Proc. Natl. Acad. Sci. U.S.A.* **107**, 529 (2009).
16. Y. Nishino, Y. Takahashi, N. Imamoto, T. Ishikawa, and K. Maeshima, *Phys. Rev. Lett.* **102**, 018101 (2009).
17. H. N. Chapman, and K. A. Nugent, *Nat. Photonics* **4**, 833 (2010).
18. H. Jiang et al., *Proc. Natl. Acad. Sci. U.S.A.* **107**, 11234 (2010).
19. M. M. Seibert *et al.*, *Nature* **470**, 78 (2011).

20. G. Zheng, R. Horstmeyer, and C. Yang, *Nat. Photonics* **7**, 739 (2013).
21. J. Miao, T. Ishikawa, I. K. Robinson, and M. M. Murnane, *Science* **348**, 530 (2015).
22. D. F. Gardner *et al.*, *Nat. Photonics* **11**, 259 (2017).
23. M. Holler *et al.*, *Nature* **543**, 402 (2017).
24. S. Gao *et al.*, *Nat. Commun.* **8**, 163 (2017).
25. Y. Jiang *et al.*, *Nature* **559**, 343 (2018).
26. F. Pfeiffer, *Nat. Photon* **12**, 9 (2018).
27. A. Michelson *et al.*, *Science* **376**, 203 (2022).
28. A. Rana *et al.*, *Nat. Nanotechnol.* **18**, 227 (2023).
29. S. Boutet *et al.*, *J. Electron Spectros. Relat. Phenomena* **166–167**, 65 (2008).
30. C. T. Putkunz *et al.*, *Phys. Rev. Lett.* **106**, 013903 (2011).
31. T. Y. Lan, P. N. Li, and T. K. Lee, *New J. Phys.* **16**, 033016 (2014).
32. C. Kim *et al.*, *Opt. Express* **22**, 29161 (2014).
33. Y. Takayama, S. Maki-Yonekura, T. Oroguchi, M. Nakasako, and K. Yonekura, *Sci. Rep.* **5**, 8074 (2015).
34. D. Noh *et al.*, *J. Phys. Condens. Matter* **28**, 493001 (2016).
35. Y. H. Lo *et al.*, *Nat. Commun.* **9**, 1826 (2018).
36. J. Miao, D. Sayre, and H. N. Chapman, *J. Opt. Soc. Am. A* **15**, 1662 (1998).
37. Y. Shechtman *et al.*, *IEEE Signal Processing Mag.* **32**, 87 (2015).
38. F. Zernike, *Science* **121**, 345 (1955).
39. M. Born and E. Wolf, *Principles of Optics*, Pergamon Press, Oxford, 6th ed. (1980).

40. See Supplemental Material at <http://link.aps.org/supplemental/XXX> for supplemental figures, table and videos.

41. J. R. Fienup et al., *Appl. Opt.* **21**, 2758 (1982).

42. S. Marchesini et al., *Phys. Rev. B* **68**, 140101 (2003).

43. M. Pham, P. Yin, A. Rana, S. Osher, and J. Miao, *Opt. Express* **27**, 2792 (2019).

44. I. McNulty et al., *Science* **256**, 1009 (1992).

45. S. Eisebitt et al., *Nature* **432**, 885 (2014).

46. T. Popmintchev et al., *Science* **336**, 1287 (2012).

47. P. Musumeci et al., *Nucl. Instrum. Methods Phys. Res. A* **907**, 209 (2018).

Figures and Figure Captions

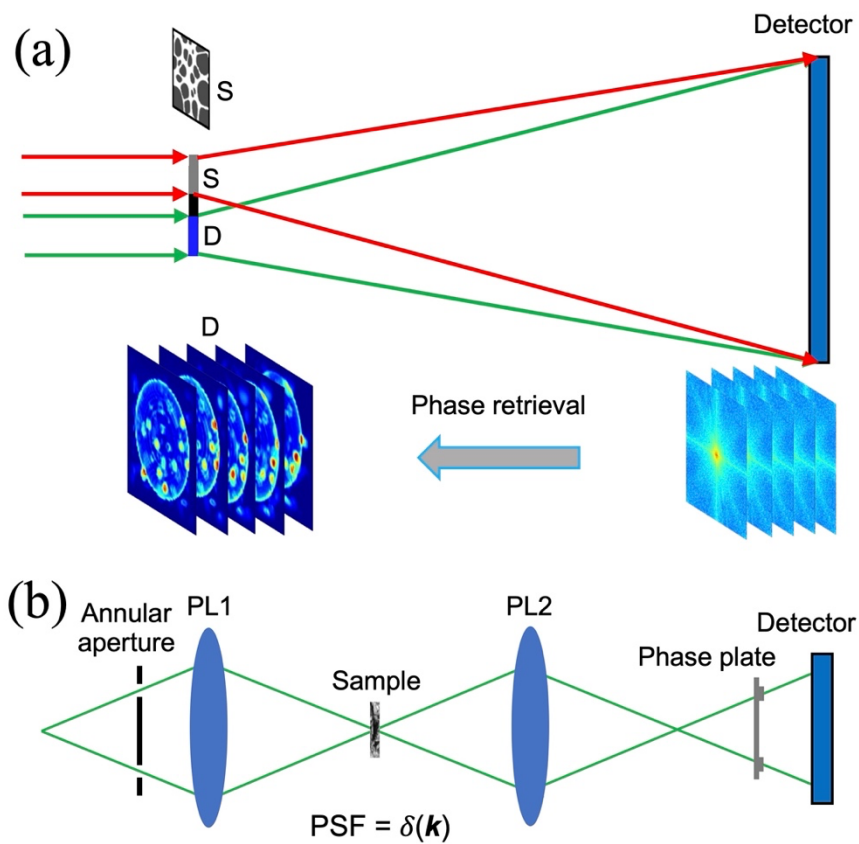


Fig. 1. Schematic of a computational microscope based on in situ CDI and a phase-contrast microscope with perfect lenses. (a) A computational microscope consists of a static (S) and a dynamic (D) structure that are coherently illuminated by a strong and a weak beam, respectively. A time-sequence diffraction patterns are collected from the coherent interference of the two beams by a detector. A time-sequence phase images are reliably reconstructed from the diffraction patterns by phase retrieval algorithms. (b) A perfect phase-contrast microscope consists of a source, an annular aperture, a first perfect lens (PL1), a sample, a second perfect lens (PL2), a phase plate, and a detector, of which the point spread function (PSF) is assumed to be a delta function.

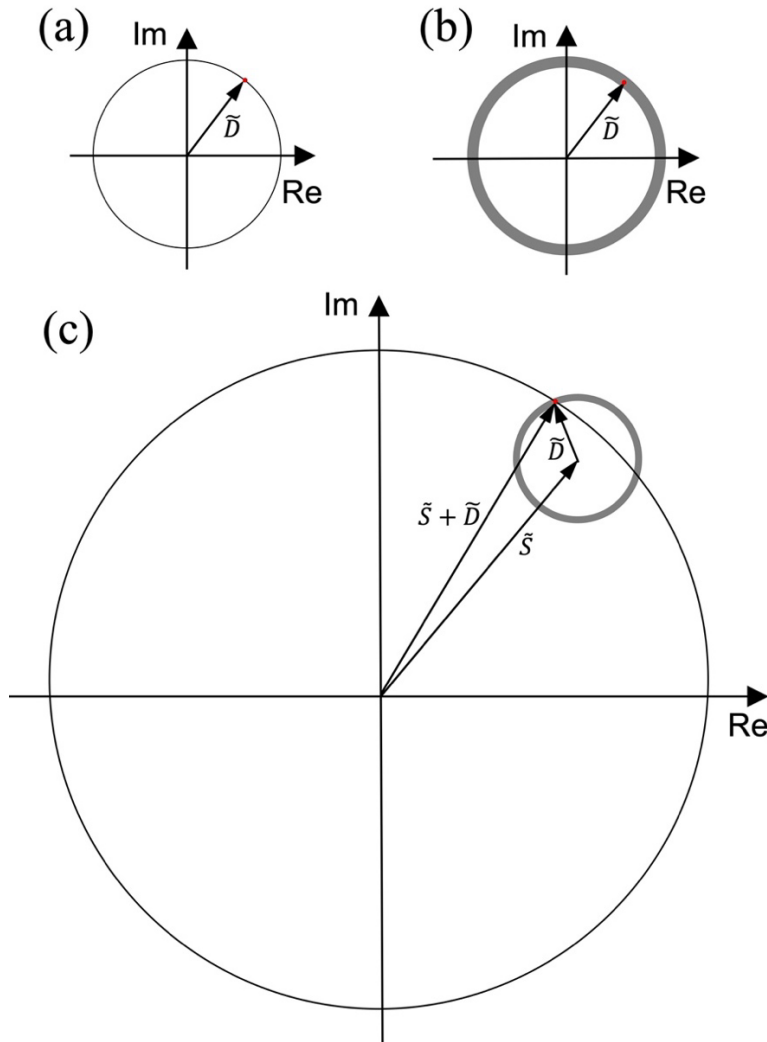


Fig. 2. CDI-based computational microscopy in the complex plane. (a) In conventional CDI, the Fourier component of each pixel in reciprocal space represents a vector, \tilde{D} , confined in a circle. With low noise and the oversampling condition satisfied [36], the correct phase (red dot) can be recovered by phase retrieval algorithms. (b) With very high noise, the circle becomes an annulus and phase retrieval algorithms are usually trapped in local minima instead of converging to the global minimum (red dot) [37]. (c) In in situ CDI, the coherent interference between a strong beam illuminating a static structure and a weak beam illuminating a dynamic structure produces a large circle in the complex plane, which intersects with a small annulus from the dynamic structure. Phase retrieval algorithms can quickly find the global minimum (red dot) instead of trapping in local minima as it becomes a convex problem.

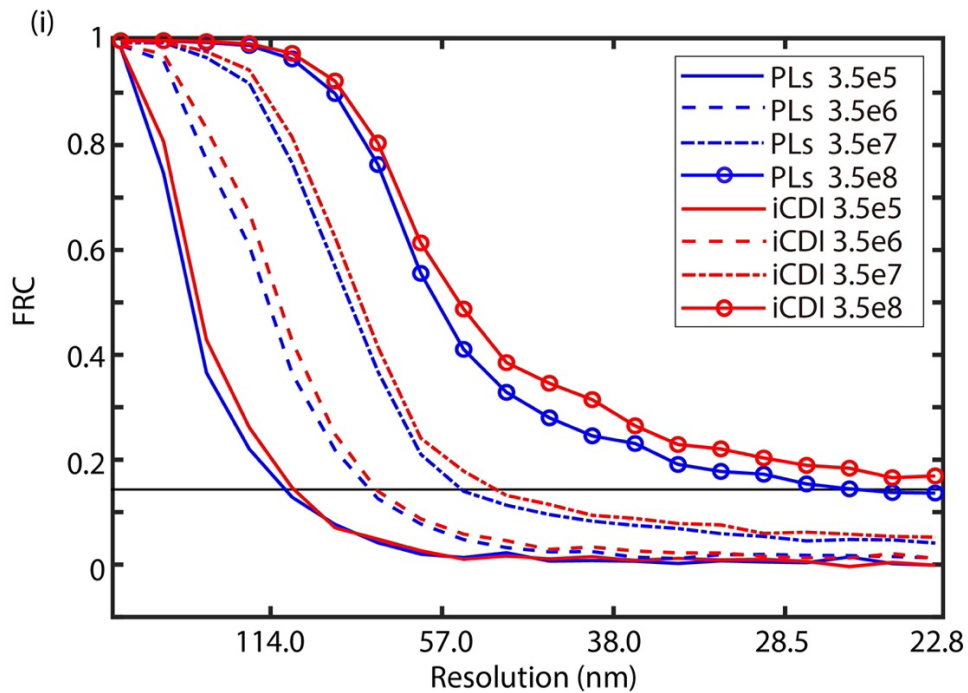
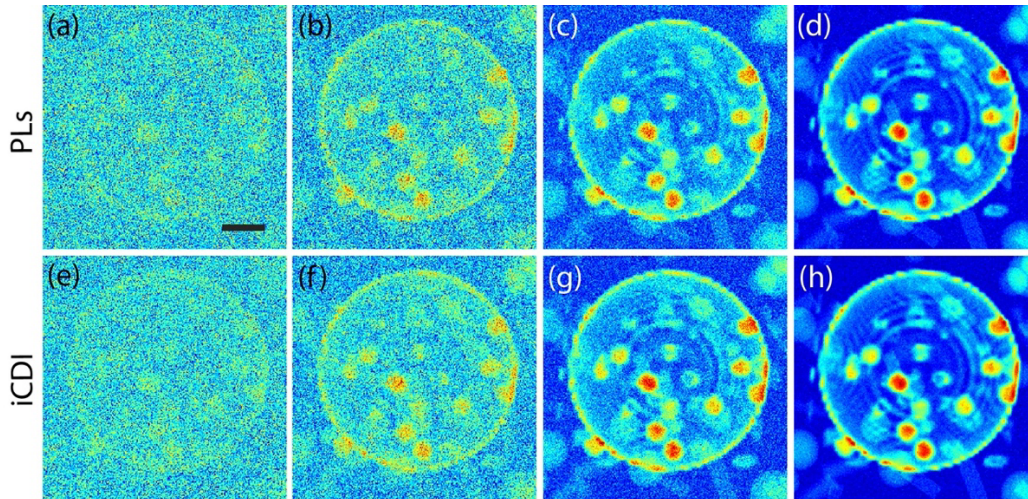


Fig. 3. Numerical experiments on phase-contrast microscopy with perfect lenses (PLs) and in situ CDI (iCDI). (a)-(d) Representative images of a 100-nm-thick dynamic biological vesicle obtained by phase-contrast microscopy with perfect lenses using an x-ray fluence of $3.5e5$, $3.5e6$, $3.5e7$, and $3.5e8$ photons/ μm^2 , respectively, corresponding to a dose of $2.75e4$, $2.75e5$, $2.75e6$, and $2.75e7$ Gy, respectively. (e)-(h) The same images reconstructed by in situ CDI with an x-ray

fluence of 3.5×10^4 , 3.5×10^5 , 3.5×10^6 , and 3.5×10^7 photons/ μm^2 , respectively. (i) Average Fourier ring correlation (FRC) curves of the 20-frame phase images obtained by perfect lenses and in situ CDI as a function of the x-ray fluence, where the FSC curves are calculated in comparison with the dynamic biological vesicle model (Supplemental Material [40], Movie S1). The black line with FRC = 0.143 indicates the resolution. Scale bar, 500 nm.

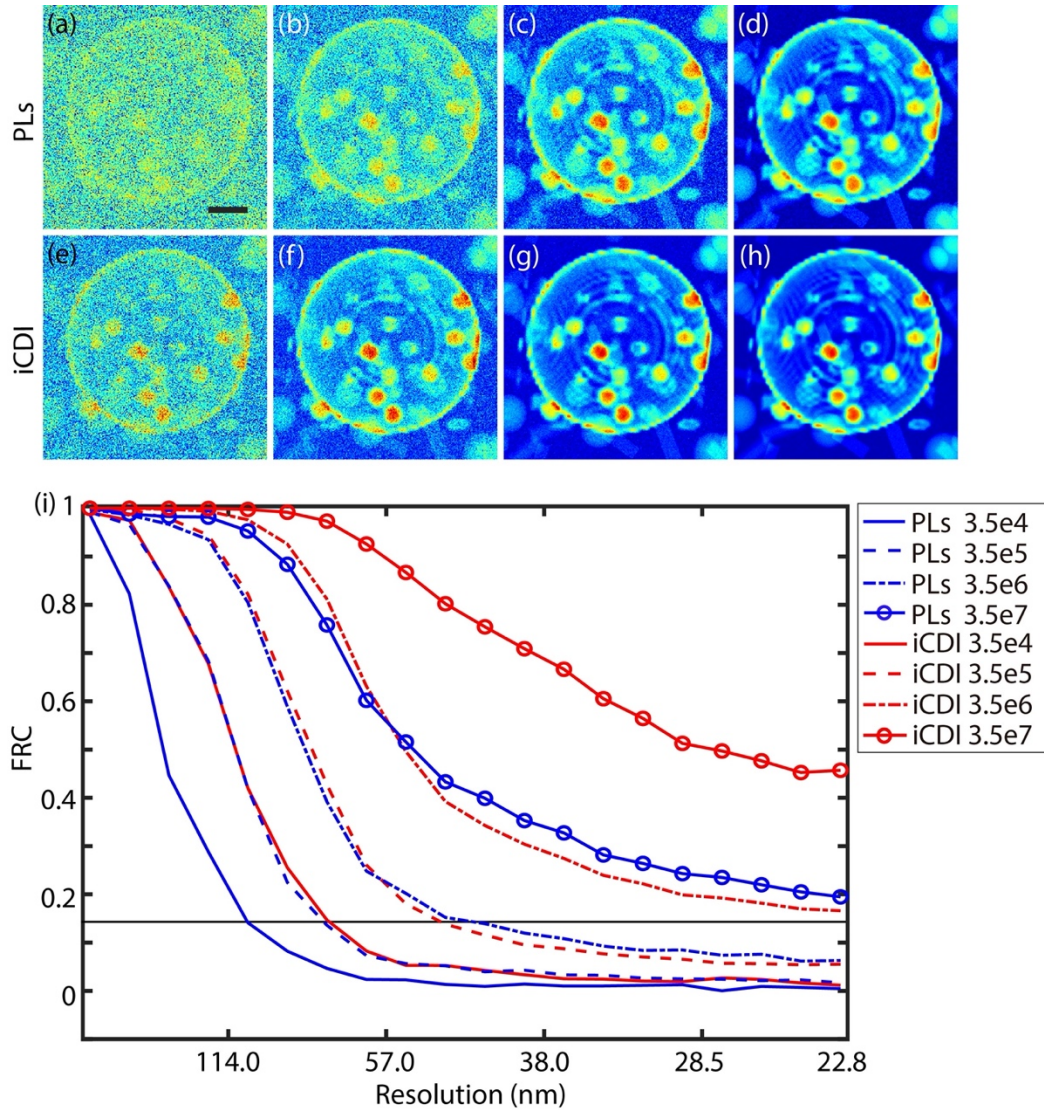


Fig. 4. Numerical experiments on absorption-contrast microscopy with perfect lenses and in situ CDI. (a)-(d) Representative images of a 1- μm -thick dynamic biological sample obtained by phase-

contrast microscopy with perfect lenses using an x-ray fluence of $3.5e4$, $3.5e5$, $3.5e6$, and $3.5e7$ photons/ μm^2 , respectively. (e)-(h) The same images reconstructed by in situ CDI with an x-ray fluence of $3.5e4$, $3.5e5$, $3.5e6$, and $3.5e7$ photons/ μm^2 , respectively. (i) Average FRC curves of the 20-frame absorption-contrast images with perfect lenses and the 20-frame phase images reconstructed by in situ CDI as a function of the x-ray fluence, where the FSC curves are calculated in comparison with the dynamic biological vesicle model. Scale bar, 500 nm.